



RESEARCH ARTICLE

Supramolecular-mediated ball-in-ball porous carbon nanospheres for ultrafast energy storage

Lei Yao^{1,2}  | Junsheng Lin^{1,3} | Yuanyuan Chen¹ | Xiujuan Li¹ | Dongrui Wang² | Haitao Yang¹ | Libo Deng³ | Zijian Zheng² 

¹College of Materials Science and Engineering, Shenzhen University, Shenzhen, P.R. China

²Laboratory for Advanced Interfacial Materials and Devices, Institute of Textiles and Clothing, The Hong Kong Polytechnic University, Hong Kong SAR, China

³College of Chemistry and Environmental Engineering, Shenzhen University, Shenzhen, P.R. China

Correspondence

Lei Yao, College of Materials Science and Engineering, Shenzhen University, Shenzhen, Guangdong 518060, P.R. China.
Email: lyao@szu.edu.cn

Libo Deng, College of Chemistry and Environmental Engineering, Shenzhen University, Shenzhen, Guangdong 518060, P.R. China.
Email: denglb@szu.edu.cn

Zijian Zheng, Laboratory for Advanced Interfacial Materials and Devices, Institute of Textiles and Clothing, The Hong Kong Polytechnic University, Hong Kong SAR, China.
Email: tczzheng@polyu.edu.hk

Funding information

Natural Science Foundation of Guangdong Province, Grant/Award Number: 2020A1515011127; Shenzhen Government's Plan of Science and Technology, Grant/Award Numbers: JCYJ20190808121407676, 20200813142301001; Shenzhen University Initiative Research Program, Grant/Award Number: 2019005; Natural Science Foundation of China, Grant/Award Number: 22178223

Abstract

Hierarchical porous carbons are the most viable electrode material for supercapacitors because of their balanced capacitive performance and chemical stability. Their pore connectivity plays a pivotal role in electrolyte transport, which is quantified by a new parameter, defined in this work as the longest possible pore separation (LPPS). Herein, we report hierarchical porous carbon nanospheres (HPC-NS) with a unique ball-in-ball structure, which is achieved by the pyrolysis of a supramolecular complex of γ -cyclodextrin (γ -CD)/PEO-PPO-PEO (F127). This approach differs from the conventional soft-templating method in that, apart from the assembly of the monomicelles that leads to the host nanospheres (approximately 300 nm), the γ -CD-containing monomicelles themselves are converted to small porous carbon nanospheres (<10 nm), which results in an ultralow LPPS of 10 nm, representing the best-known pore connectivity of the HPC family. The HPC-NS delivers a high specific capacitance (405 F g^{-1} at 1 A g^{-1} and 71% capacitance retention at 200 A g^{-1}), wide voltage window (up to 1.6 V), and simultaneously high energy and power densities (24.3 Wh kg^{-1} at a power density of 151 W kg^{-1} and 9 Wh kg^{-1} at 10^5 W kg^{-1}) in aqueous electrolytes. This new strategy boosts the development of porous carbon electrodes for aqueous supercapacitors with simultaneously high power and energy densities.

KEYWORDS

hierarchical porous carbon, pore connectivity, supramolecular, ultrafast energy storage

This is an open access article under the terms of the Creative Commons Attribution License, which permits use, distribution and reproduction in any medium, provided the original work is properly cited.

© 2021 The Authors. *InfoMat* published by UESTC and John Wiley & Sons Australia, Ltd.

1 | INTRODUCTION

Supercapacitors, which store energy through electrostatic adsorption of ions on their electrode surface, have attracted enormous interest, particularly as researchers are focusing on improved sustainability, owing to their high charge/discharge rate and unrivaled long-term stability and safety among the various electrochemical energy storage devices.^{1–5} Porous carbonaceous materials are viable electrode materials and are extensively used in commercial supercapacitors. Their pore structure profoundly influences all metrics of the device, such as the power and energy densities. Hierarchical porous carbons (HPCs), that is, those containing micro-, meso-, and macropores, are in the spotlight among the broad carbon family for next-generation supercapacitors. It is well-documented that micropores provide predominant adsorption sites, whereas meso- and macropores allow efficient mass transport.^{6–8} Early efforts have focused on creating hierarchical pores using different precursors such as biomass, polymers, and metal–organic frameworks.^{9–13} More recent efforts have been dedicated to controlling the pore size distribution, volume fraction of pores, and morphology of HPC, leading to promising capacitance and energy density, such as 313 F g^{−1} for three-dimensional HPC (3D-HPC) in KOH electrolyte¹⁴ and an energy density of 139 Wh kg^{−1} for two-dimensional HPC (2D-HPC) in an ionic liquid electrolyte developed by our group.¹⁵ However, despite the advantageous capacitance of supercapacitors achieved at relatively low current densities, their power density, along with other metrics, requires further improvement to meet future demands.

A recent theoretical study demonstrated that the interpore connectivity has a profound effect on energy storage and that not all hierarchical pores are equally beneficial.¹⁶ Electrolyte transport is efficient only when the pores are well-percolated, whereas isolated pores are inaccessible, especially at high current densities. A number of recent experimental studies also pointed out the importance of interpore connections in the performance of porous carbon supercapacitors,^{17–19} but direct characterization of pore connectivity at the micropore scale is still a great challenge and remains less explored. A parameter quantifying the connectivity of pores would allow a better understanding of the energy storage mechanism in all porous carbon materials. In this work, we propose that, when no experimental quantification of the interpore connectivity is available, the size of the primary unit that composes the interconnected 3D-HPC, denoted as the longest possible pore separation (LPPS), can be used to characterize the pore percolation and serve as a guide to design high-performance HPC.

The most prominent method for preparing porous carbon is physical/chemical activation of an existing carbon

and may be combined with pyrolysis of an organic precursor, through which multiple-length-scale pores are generated by etching of the less-stable domain.^{20–26} This process often results in high surface areas but lacks the capability for pore tailoring. Soft templating, on the other hand, usually yields ordered and uniform pores. This approach generally involves the self-assembly of an amphiphilic template into monomicelles, followed by polymerization of the carbon source to further assemble into larger nanospheres.^{27–32} Upon carbonization, the collapse of the monomicelles that are encapsulated in the supramolecular complex yields mesopores, with the pore size depending on the molecular weight of the template.^{28–30} The carbonized nanospheres can further serve as a building block of interconnected 3D-HPC, which has a typical LPPS above 20 nm (equal to the size of an individual sphere).²⁹ A shorter LPPS can be created by designing interconnected sub-units inside each nanosphere building block in order to reduce the size of the primary unit that constitutes the 3D-HPC. This work demonstrates that the smallest unit is monomicelle-derived balls inside the carbon nanospheres.

In this study, we prepared a novel type of HPC nanospheres (HPC-NS) via a soft-templating method using F127 as the template and γ -cyclodextrin (γ -CD) as the carbon source (Figure 1A). A unique ball-in-ball configuration was obtained owing to the host–guest interaction between the hydrophobic cavity of γ -CD and F127, which has not yet been reported in previous studies involving the soft-templating process. Internal small carbon balls with diameters below 10 nm, also denoted as carbon quantum dots (CQDs), were formed by the carbonization of γ -CD/F127 monomicelles during the facile conversion of CD into stable sp² carbons. Abundant micro- and mesopores were generated in the CQDs owing to the decomposition of F127 chains. Host carbon balls were formed by the polymerization of γ -CD during the hydrothermal process, followed by high-temperature carbonization. This ball-in-ball structure afforded an LPPS at the sub-10 nm scale, which was the lowest pore separation measured to date and was one-tenth that of the conventional 3D-HPC built using pure γ -CD-derived nanospheres (denoted as PC-NS) (Figure 1B). The improved pore connectivity and facilitated ion transport enabled extraordinary rate performance in supercapacitors, delivering both high power density (up to 10⁵ W kg^{−1} or a capacitance of 135 F g^{−1} at 250 A g^{−1}) and high energy density (24.3 Wh kg^{−1} at 151 W kg^{−1}) in an aqueous electrolyte.

2 | RESULTS AND DISCUSSION

The HPC-NS was prepared by pyrolysis of a mixture of the γ -CD/F127 supramolecular complex and KOH at

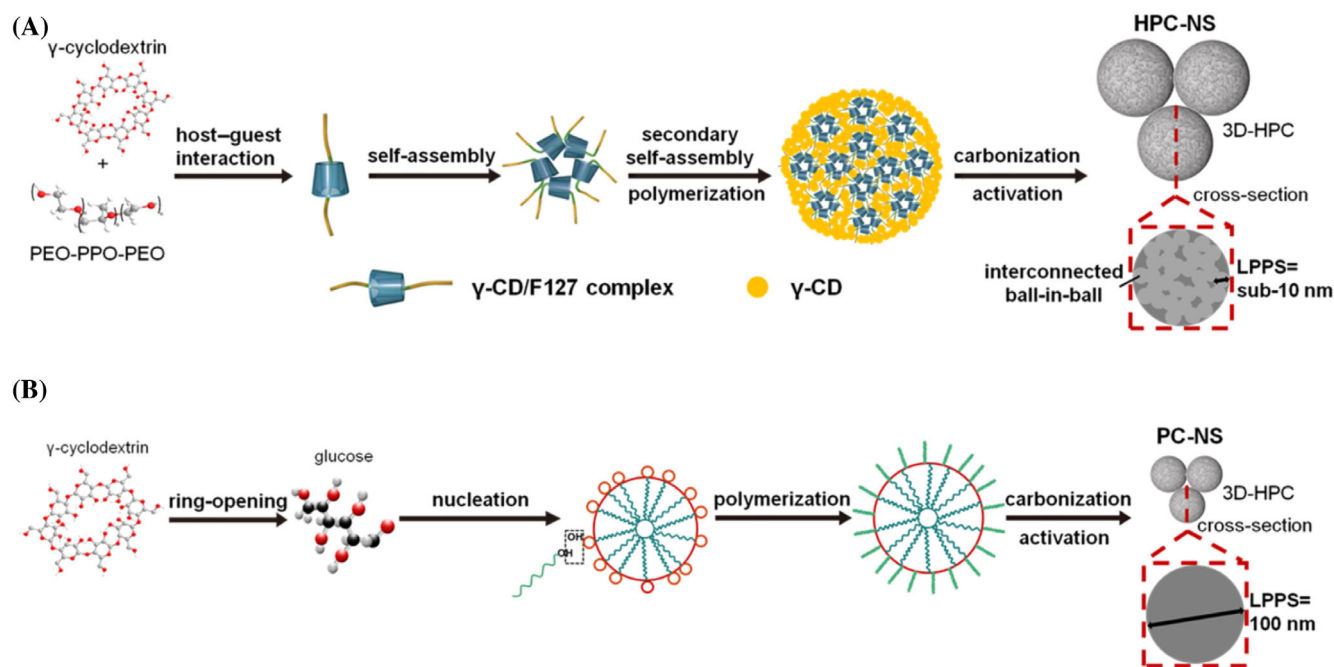


FIGURE 1 Illustration of the formation mechanism for two types of 3D-HPC composed of carbon nanospheres: (A) HPC-NS with a low LPPS (high interpore connectivity). (B) PC-NS with a high LPPS (poor interpore connectivity)

700°C, during which the supramolecular carbon source was formed by the self-assembly of γ -CD and F127. γ -CD is a cyclic oligosaccharide consisting of eight glucose units, which can be converted to a graphitic structure upon carbonization that, in turn, endows the pyrolytic carbon with high electrical conductivity (145 S m^{-1} for the final HPC-NS).³³ Upon mixing with γ -CD, the polypropylene oxide (PPO) block chain of F127 can penetrate into the inner cavity of γ -CD through the hydrophobic attraction host-guest interaction,³⁴ and then the γ -CD/F127 complex self-assembles into the spherical monomicelles.²⁸ During the subsequent hydrothermal treatment, the monomicelles further coalesce into larger spheres through both self-polymerization of the free γ -CDs (i.e., those unbound by F127) and the reaction between γ -CD and F127, as demonstrated in our recent study,³⁵ giving rise to a hierarchical structure consisting of γ -CD/F127 monomicelles embedded in the polymerized γ -CD matrix (Figure 1A). Systematic x-ray diffraction (XRD), Fourier transform infrared (FTIR), and nuclear magnetic resonance (NMR) analyses confirmed the host-guest interaction and the tight-fit channel-type configuration of the γ -CD/F127 complex (Figure S1A–C). The hydrothermal carbonization (HTC) of the γ -CD/F127 complex resulted in intermediate nanospheres with mixed sp^3 and sp^2 hybridized carbon with an average diameter of 300 nm (Figure S1D) and an oxygen content of 23.5 at.% as determined by x-ray photoelectron spectroscopy (XPS, Figure S2).

The morphology of the intermediate nanospheres was retained and the particle diameter decreased slightly after carbonization/activation at 700°C (the morphology is shown in Figure 2A and the size distribution histogram is shown in Figure S3). Transmission electron microscopy (TEM) revealed a turbostratic structure comprising small graphitic domains with a low stacking order in HPC-NS (Figure 2B), which was in agreement with the XRD results (Figure S4). It is particularly interesting to note from the high-resolution TEM images that bright nanodomains with an average width of 5–10 nm were dispersed in the host carbon nanospheres (Figure 2C–F). Elemental mapping indicated a lower carbon density in these domains compared with the host carbon matrix (Figure 2G–I). To determine whether the bright nanodomains were void or solid, over 100 specimens with a thickness of approximately 10 nm were prepared using an ultramicrotome and were carefully inspected under aberration-corrected TEM (ACTEM), yet no through-holes were observed. Therefore, these nanodomains were identified as highly porous CQDs that resided in the host carbon nanospheres, yielding a unique ball-in-ball configuration. In addition, these porous inner balls were well connected (highlighted by dotted lines in Figure 2D), and thus the pores were connected to each other at a sub-10 nm scale (i.e., the material had an LPPS of 10 nm). Such good pore connectivity can remarkably enhance electrolyte transport within the pore network.

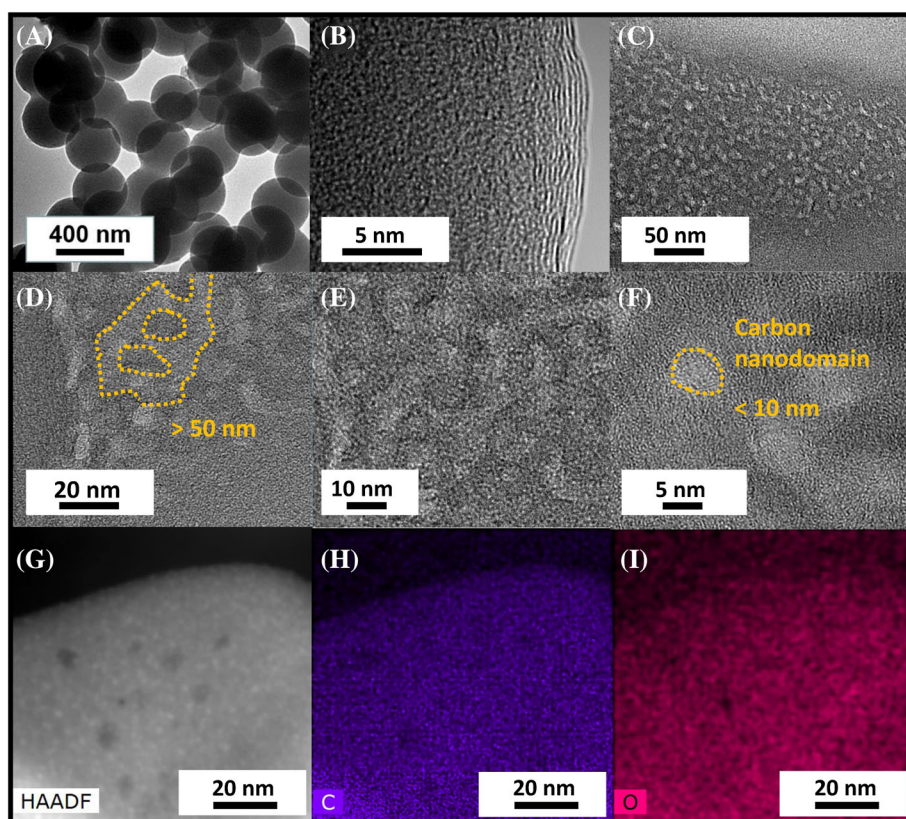


FIGURE 2 The ball-in-ball hierarchical porous structure of HPC-NS: (A) TEM image. (B) High-resolution TEM image. (C–F) TEM images of cross-sectional slice. (G) HAADF image of cross-sectional slice. (H,I) Elemental scanning mapping image of carbon and oxygen elements

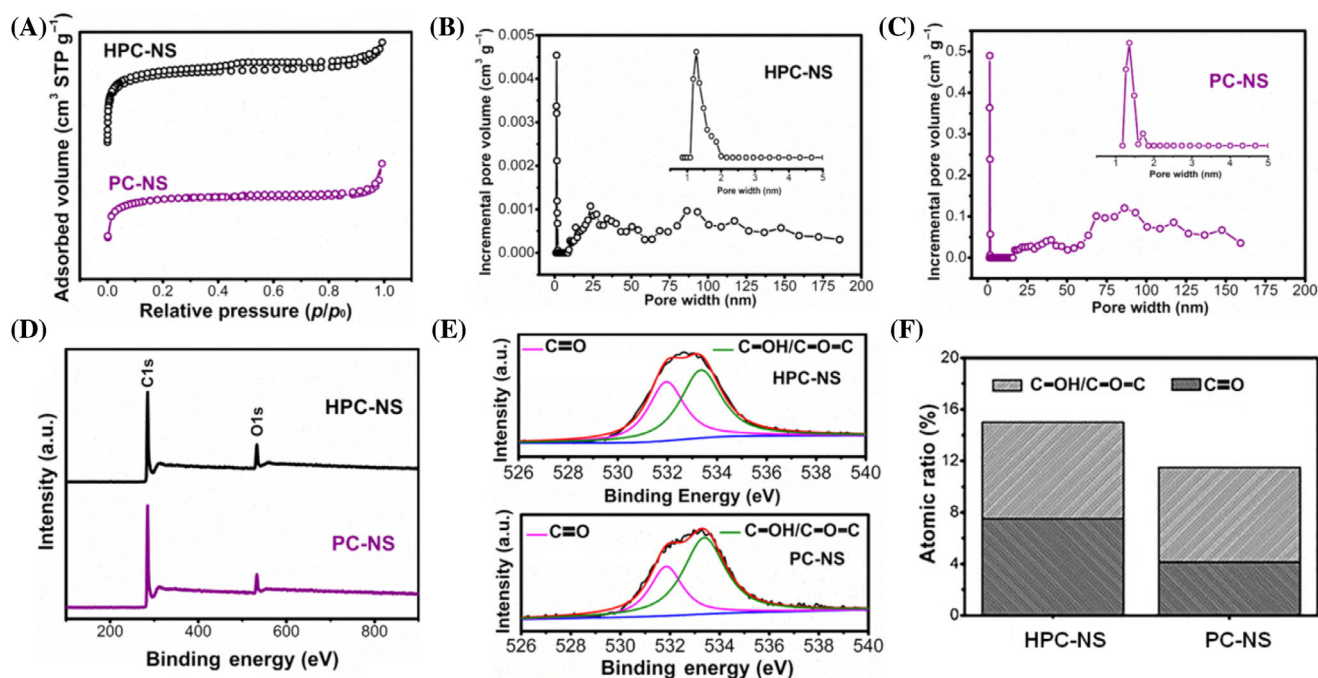


FIGURE 3 Structural and elemental characterization of HPC-NS and PC-NS: (A) The N_2 adsorption–desorption curves. (B) Pore size distribution of HPC-NS. (C) Pore size distribution of PC-NS. (D) XPS survey spectra of HPC-NS and PC-NS. (E) The high-resolution O 1s peak of HPC-NS and PC-NS. (F) The atomic percentage of oxygen element and its two configurations

To investigate the formation mechanism of the unique pore structure of HPC-NS, nitrogen adsorption/desorption tests were conducted. The HTC product prior to high-temperature carbonization exhibited only meso- and macropores in the range of 15–60 nm with a surface area of $9 \text{ m}^2 \text{ g}^{-1}$ (Figure S2B). Carbonization of the HTC product at 700°C without KOH activation resulted in a hierarchical porous structure and a specific surface area of $765 \text{ m}^2 \text{ g}^{-1}$ (Figure S5A). Further activation with a small amount of KOH (HTC product: KOH = 3:1) at the same temperature did not significantly change the surface area ($777 \text{ m}^2 \text{ g}^{-1}$ for HPC-NS, Figure 3A). However, HPC-NS exhibited a larger volume fraction of pores in the range of 7–20 nm compared with the unactivated carbon nanospheres (Figures 3B and S5B). The different pore size distributions indicate that micropores in the unactivated samples were associated with the decomposition of the F127 chains confined in γ -CD. Upon KOH activation, unstable regions were etched off, which enlarged the micropores and increased the pore connectivity of the carbon nanospheres. Meanwhile, KOH etching also created new micropores, which compensated for the reduction in the specific surface area. Thus, the one-pot KOH activation and carbonization process were critical for the generation of well-defined pore connectivity in the internal carbon sphere, which provided a highly accessible surface area and short diffusion pathways for the electrolyte ions.

In comparison, HTC treatment was also conducted with neat γ -CD solution without F127, during which CD was converted to glucose and subsequently underwent ring-opening/dehydration and polymerization/carbonization (Figure 1B). The obtained nanospheres exhibited an average diameter of 100 nm (Figure S6), which was substantially smaller than those prepared from the γ -CD/F127 complex. The subsequent carbonization and activation of the HTC product led to carbon nanospheres with a homogenous phase across the whole particle without a ball-in-ball heterostructure (Figure S7), which is denoted as PC-NS. In this case, the LPPS was approximately 100 nm. To confirm the effect of F127 on the assemble and carbonization behavior of cyclodextrin, we also conducted the preparation using different amounts of F127 while keeping the cyclodextrin constant. It was found the diameter increased and the surface area of the final carbon nanospheres decreased slightly with the increasing amount of F127 used (Figure S8 and Table S1). The increase of the diameter could be understood that, during hydrothermal treatment of the supramolecular complex and apart from self-polymerization of CD, polymerization also occurred between the monomicelles through both non-covalent and covalent reactions, leading to a dynamically cross-linked network. Compared with HPC-NS, PC-NS showed a similar surface area of $749 \text{ m}^2 \text{ g}^{-1}$ (Figure 3A).

Furthermore, it also showed a hierarchically porous structure, but the pore volume fraction in the mesoscopic range, especially those between 7 and 17 nm, was much lower than that of HPC-NS (Figure 3C). It is thus concluded that F127, which led to the supramolecular complex, also played an important role in forming the ball-in-ball configuration and good pore connectivity in HPC-NS. Specifically, the carbonization of the polymeric cyclodextrin backbone resulted in the host carbon nanospheres, whereas the pyrolysis of F127/ γ -CD monomicelles gave rise to CQDs with interconnected pores.

In addition to the significant difference in the phase structure and pore size distribution between HPC-NS and PC-NS, the XPS characterization of the surface composition also revealed a higher content of oxygen in HPC-NS (14.9 at.%) than that in PC-NS (9.5 at.%, Figure 3D). Figure 3E displays the high-resolution O 1s spectra of HPC-NS and PC-NS, in which the peaks with binding energies of 532 and 533 eV represented C=O quinone groups and C—OH phenol groups or C—O—C ether groups, respectively.³⁶ Moreover, the fraction of quinone oxygen in HPC-NS (7.2 at.%) was remarkably higher than that in PC-NS (4.5 at.%), indicating that F127 also influenced the surface chemistry of the pyrolytic carbon nanospheres (Figure 3F). Elemental analysis of the bulk of HPC-NS suggests an overall oxygen content of 4.5 at.%, indicating a lower extent of KOH activation in the interior region. Nevertheless, these oxygen-containing groups (e.g., quinone groups) may increase electrochemical capacitance through fast redox reactions.^{37–39} Therefore, the combination of a unique pore hierarchy and highly oxygenated surface in the encapsulated CQDs endowed HPC-NS with a promising electrochemical performance as supercapacitor electrodes.

As discussed above, the micropores in PC-NS were not sufficiently connected (Figure 4A), which is an issue that hinders the ion transport energy storage for most porous carbon nanospheres previously reported. In contrast, the host–guest interaction between F127 and γ -CD led to optimal reactivity and thermal stability of the building units (monomicelles), which affords HPC-NS an enhanced connectivity of pores and a faster transportation pathway for ions. To evaluate the accessibility of micropores in these two materials, HPC-NS and PC-NS were immersed in NaOH solution and thoroughly dried, and solid-state NMR spectra were acquired. The ^{23}Na peak located at -1.2 ppm corresponded to the free electrolyte molecules (or weakly bonded electrolytes), whereas the appearance of an extra peak with a higher shift was ascribed to the electrolytes confined in the micropores or small mesopores (Figure 4B). When the NaOH electrolyte penetrated into the micropores, the delocalized carbon π electrons circulated in the

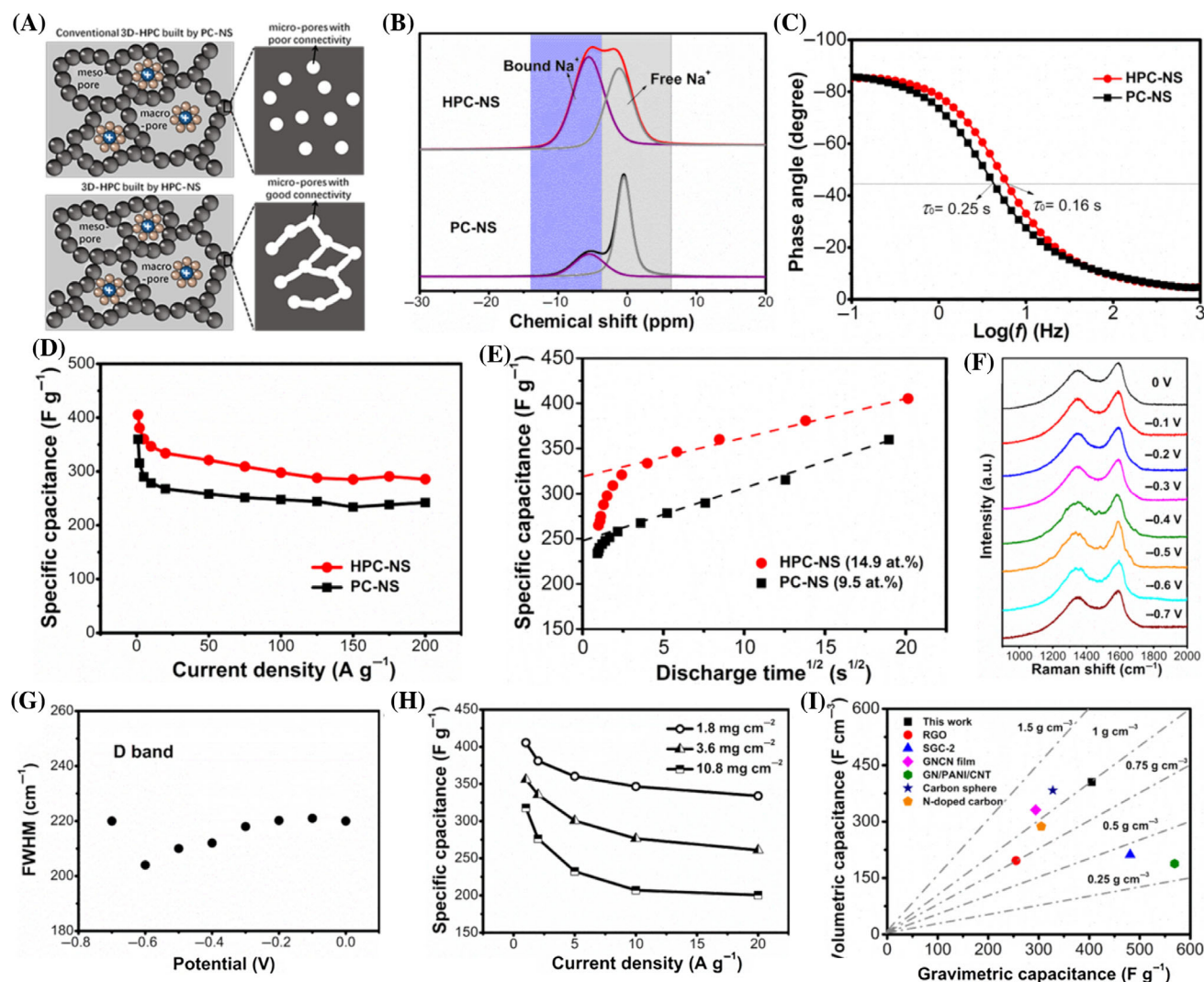


FIGURE 4 The electrochemical properties of the two 3D-HPC electrodes tested using a three-electrode system: (A) Schematic diagram illustrating the pore structure of two types of 3D-HPC. (B) ^{23}Na NMR spectra for the NaOH-impregnated porous carbons. (C) Bode plots. (D) The specific capacitance as a function of the current density. (E) Capacitance versus square root of discharge time. Extrapolated intercept capacitance is the rate-independent capacitance k_1 , and the remainder is the diffusion-controlled capacitance. (F) In situ Raman spectra of HPC-NS charged at different potentials. (G) The dependence of FWHM of the D-band on the potential for HPC-NS. (H) The specific capacitance as a function of the current density for HPC-NS electrodes with different mass loadings. (I) Comparison of the gravimetric and volumetric capacitances of HPC-NS with other carbon materials.^{45,48–52} Electrolyte: 6 M KOH

presence of an applied magnetic field, which induced a local magnetic field and shielded the nearby nuclei, resulting in an upward shift of the ^{23}Na peak. This shielding effect was only appreciable in micropores or small mesopores.^{40–42} The shift of the ^{23}Na peak for the micropore-trapped ions in HPC-NS ($\Delta\delta = 5.7$ ppm) was larger than that in PC-NS ($\Delta\delta = 5.4$ ppm), which suggests a stronger shielding effect by pores in the former (Figure 4B). Moreover, the fraction of the strongly adsorbed electrolyte was determined from the two ^{23}Na peaks, which were 50.9% for HPC-NS and 37.3% for PC-NS. These results indicated better accessibility of the micropores in the HPC-NS. The charging/discharging kinetics of the

carbon nanospheres were further evaluated using electrochemical impedance spectroscopy (EIS) in a three-electrode system with a 6 M KOH electrolyte (Figure 4C). The time constant τ_0 ($\tau_0 = 1/f_0$, f_0 is the characteristic frequency at the phase angle of -45°) was derived from the Bode plots and was 0.16 s for HPC-NS and 0.32 s for PC-NS, further confirming a faster ion transport and charge transfer in HPC-NS.

The efficient transport of ions and electrons in the HPC-NS endowed it with extraordinary capacitance and a high rate performance. It could be charged and discharged even at a current density of up to 200 A g^{-1} with a high Coulombic efficiency ($>98\%$) (Figure S9).

Specifically, the capacitance of HPC-NS was 405 F g^{-1} at 1 A g^{-1} and exhibited 287 F g^{-1} at 200 A g^{-1} , which represented 71% of its value at 1 A g^{-1} (Figure 4D). These values were higher than those for PC-NS, and only a few reports have demonstrated charging/discharging ability at such a high current.^{43–45} The apparent capacitance C can be deconvolved into the rate-independent component k_1 and the diffusion-limited component controlled by the scanning rate ν ($\nu = t^{-1}$, where t represents the discharging time), which is described by the equation $C = k_1 + k_2\nu^{-1/2}$.⁴⁶ Figure 4E shows the capacitance as a function of $\nu^{-1/2}$, from which k_1 values were determined (the intercept at $t^{1/2} = \nu^{-1/2} = 0$) to be approximately 319 F g^{-1} for HPC-NS and 248 F g^{-1} for PC-NS. For porous carbon materials, rate-independent capacitance is predominantly attributed to electric double layer capacitance (EDLC),⁴⁶ which is related to their specific surface area. HPC-NS possesses similar specific surface areas with PC-NS but a significantly higher content of oxygen and k_1 value, indicating that the rate-independent capacitance for HPC-NS contains both EDLC characteristics and pseudocapacitance originating from redox reactions. The good pore-connection and fast ion/charge conducting characteristics of HPC-NS allow facile redox reactions for oxygen-containing functional groups.

The fast redox reactions that occurred during the charging process of HPC-NS were further verified using in situ Raman spectroscopy (Figure S10). Figure 4F shows the Raman spectra acquired at different potentials that were built by charging at 0.5 A g^{-1} . A clear response of the Raman spectrum to an increase in the negative potential was observed. The initially smooth Raman spectrum became noisy in the potential range from -0.4 to -0.6 V (vs. Ag), possibly due to structural perturbation in the electrode. The spectrum became smooth again with a further increase in negative potential. The potential-dependent smoothness of the Raman spectrum was reversible during the charge/discharge test over five cycles, indicating good reversibility of the electrochemical process. Moreover, the full width at half maximum (FWHM) of the D-band decreased as the potential increased from -0.3 to -0.6 V , and it reverted to the value held at 0 V when the charging potential was further increased to -0.7 V (Figure 4G). The variation in the FWHM of the D-band is associated with the reaction of oxygen-containing functional groups, such as quinone, in HPC-NS.⁴⁷

The fast charging/discharging kinetics of HPC-NS also enabled impressive performance at high mass loadings. As the mass loading of active materials deposited on the nickel foam was increased up to 10.8 mg cm^{-2} (which is a typical mass loading for commercial devices), the electrode retained a specific capacitance of 320 F g^{-1}

at 1 A g^{-1} (Figure 4H), demonstrating its potential for practical application at a high electrode thickness. Furthermore, HPC-NS exhibited a high packing density of approximately 1 g cm^{-3} and, hence, a high volumetric capacitance (405 F cm^{-3}) and power density (Figure 4I), which is comparable to state-of-the-art results for carbonaceous materials and is of particular significance for applications in compact electronics.^{45,48–52}

To determine the electrochemically stable potential window of HPC-NS, the electrode potentiostatically dwelled at different potentials for 10 min in a 6 M KOH electrolyte using a three-electrode system, and the current was recorded. Figure 5A shows the dwelled current versus the potential of the HPC-NS. The potential at which the current increases abruptly at the negative and positive electrodes (marked by the black and red dashed lines) indicates the lower and upper potential limit, respectively.⁵³ Therefore, the theoretical electrochemically stable potential window was 1.5 V for HPC-NS in this aqueous electrolyte and a symmetric coin-type supercapacitor is expected to be operable at a voltage window up to 1.5 V (Figure 5B). However, slight distortion in the galvanostatic charge–discharge (GCD) curves can be seen when the voltage exceeds 1.2 V (Figure S11A). The long-term cycling stability of the device under different voltage windows was further evaluated (Figure 5C). The KOH-based device displayed a robust cycling stability within 1.2 V , retaining 95% of its initial capacitance after 10 000 cycles at 5 A g^{-1} . When operated at 1.5 V , the capacitance degraded by approximately 32% after 2000 cycles. Hence, the practical voltage window of the HPC-NS symmetric supercapacitor was determined to be 1.2 V , indicating that the electrochemically stable voltage window of the HPC-NS-based device was lower than that determined using the three-electrode system. The underexploited voltage window in a symmetric supercapacitor is common for carbons rich in heteroatoms, which would exert an unstable surface charge on the electrode.^{53,54} An even higher voltage window (up to 1.6 V) was achieved using larger ions Li_2SO_4 as the electrolyte, as evident from the high Coulombic efficiency of the GCD curves (Figure S11B). In the case of the Li_2SO_4 -based supercapacitor, only a 9% decay of the capacitance was observed after 10 000 cycles of charge and discharge at 5 A g^{-1} within 1.6 V (Figure 5C). The excellent stability was also confirmed by SEM inspection into the electrode after the long-term cycling test, which revealed intact carbon nanospheres with diameters similar to those prior to the cycling test (Figure S12).

The advantageous rate performance of HPC-NS evident during the three-electrode tests was also observed in practical supercapacitors, up to 1.2 V for the KOH system and 1.6 V for the Li_2SO_4 system, as indicated by the

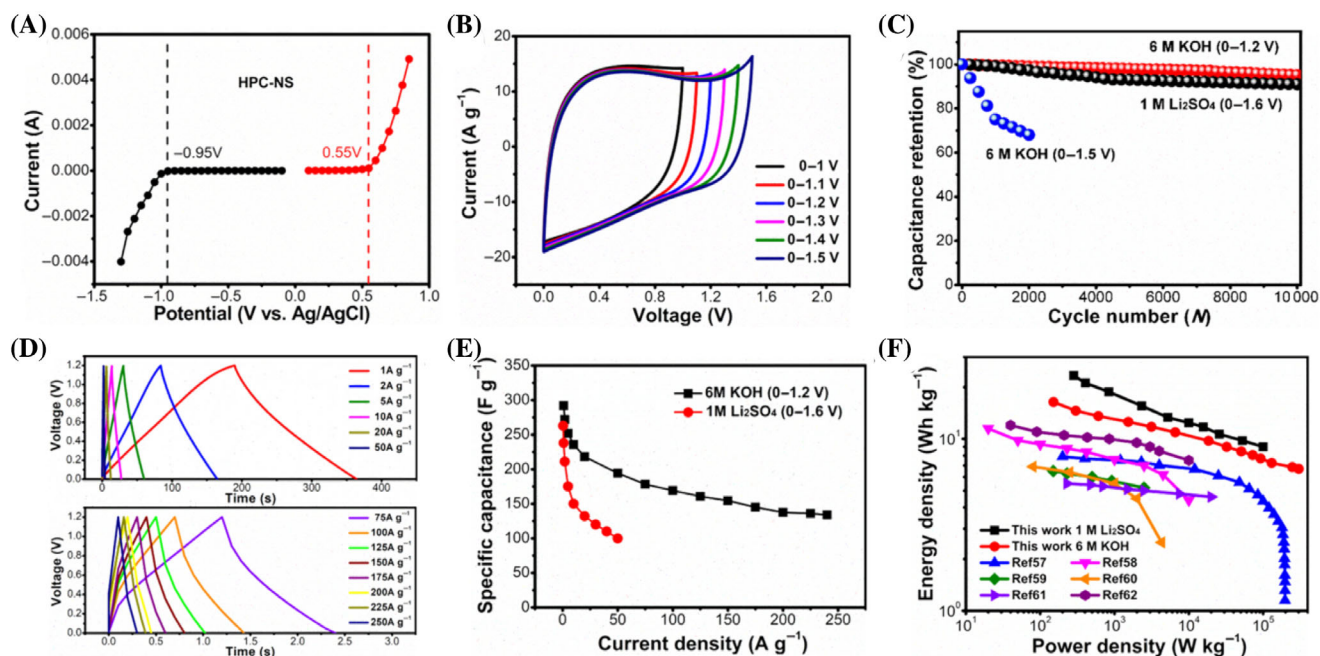


FIGURE 5 The electrochemical properties of HPC-NS-based coin-type supercapacitor using different electrolytes: (A) The current of the electrode potentiostatically dwelled for 10 min at different potentials. The dashed black line and dashed red line represent the lower and upper limit for the potential, respectively. (B) CV curves measured under different voltage windows at 100 mV s^{-1} using 6 M KOH electrolyte. (C) Cyclic stability of the supercapacitor using 6 M KOH and 1 M Li_2SO_4 electrolyte at 5 A g^{-1} , respectively. (D) GCD curves of HPC-NS coin-type supercapacitor measured at different current densities using 6 M KOH electrolyte. (E) Capacitance retention of supercapacitor using 6 M KOH and 1 M Li_2SO_4 electrolyte. (F) Ragone plot for supercapacitor using 6 M KOH and 1 M Li_2SO_4 electrolyte and a comparison with literature data^{57–62}

quasi-rectangular cyclic voltammetry (CV) curves at a scan rate up to 2 V s^{-1} (Figure S13) and the isosceles triangle behavior for the GCD curves, even at 250 A g^{-1} (Figure 5D). The specific capacitance of an HPC-NS coin-type supercapacitor tested in a KOH-based electrolyte at 1 A g^{-1} was 292 F g^{-1} (Figure 5E), which was comparable with the leading results for various porous carbon materials reported in the literature.^{14,15,55,56} The device still exhibited a capacitance of 135 F g^{-1} at a current density of 250 A g^{-1} , manifesting an extraordinary rate performance. Achieving a high capacitance at such a current density is extremely challenging and has only been reported with a few carbonaceous materials.¹⁴ When tested in a Li_2SO_4 electrolyte, the capacitance was 263 F g^{-1} at 0.5 A g^{-1} (Figure S14), which was also higher than the leading results for Li_2SO_4 -based supercapacitors currently reported.^{57–59} As expected, the rate performance of the Li_2SO_4 system was inferior to that of the KOH system due to the higher charge transfer resistance of the former electrolyte (Figures 5E and S15).

The large voltage window, high capacitance, and impressive rate performance endowed the HPC-NS-based supercapacitor with both high energy and power densities. The Ragone plots show the highest energy density of 23.36 Wh kg^{-1} at 151 W kg^{-1} for supercapacitors using

the Li_2SO_4 electrolyte. It is worth noting that the energy density still retained 9 Wh kg^{-1} when the power density was increased to an ultrahigh value of 10^5 W kg^{-1} (Figure 5F). The energy density and maximum power density in this work were higher than those of state-of-the-art aqueous supercapacitors based on a carbon electrode material,^{57–62} and thus suitability for various potential applications, such as harvesting energy at high speeds, is expected for our HPC-NS.

3 | CONCLUSION

In conclusion, HPC-NS with a low LPPS, moderate specific surface area, and high packing density was prepared using a CD-based supramolecular complex as the carbon source. The combination of the structural hierarchy with the highly oxygenated surface enables HPC-NS to be a good candidate for supercapacitor electrodes in several aspects. First, the good pore connectivity at the sub-10 nm scale in the carbon nanospheres, which has not been previously reported, leads to a high accessible surface area, as well as a fast ion and charge transport network. Second, the highly oxygenated groups on the surface enable fast redox reactions, resulting in a high pseudocapacitance and wide voltage window.

These carbon nanospheres exhibited a volumetric capacitance of 405 F cm^{-3} , an energy density of 23.36 Wh kg^{-1} at 151 W kg^{-1} , and 9 Wh kg^{-1} at an ultrahigh power density of 10^5 W kg^{-1} in a Li_2SO_4 electrolyte. The host-guest interaction between the carbon source (host) and the soft template (guest) tailored the supramolecular assembly, which played an important role in the carbonization behavior and resulted in a unique ball-in-ball structure. The interconnected sub-units, that is, the porous CQDs, in the carbon nanospheres led to a shorter LPPS and, hence, better pore connectivity. The supramolecular-mediated soft-templating method provides a universal strategy for fabricating functional hierarchical porous carbon nanomaterials. This is expected to open new doors to material innovation with modified porous carbon nanomaterials and their broad applications in electrocatalysts (e.g., for oxygen evolution/reduction reactions), rechargeable Li^+/Na^+ batteries, and other sustainable charging applications.

4 | EXPERIMENTAL

4.1 | Chemicals

γ -CD, F127, KOH, Li_2SO_4 , acetylene black, and polytetrafluoroethylene (PTFE) were purchased from Macklin Reagent Co. and used without further purification.

4.2 | Preparation of HPC-NS

Exactly 2.0 g γ -CD and 0.25 g F127 were added to deionized water (120 ml) and stirred at room temperature for 12 h. The obtained solution was then transferred to a Teflon-lined stainless-steel autoclave, which was then sealed and maintained at 220°C for 12 h. The products were filtered, rinsed with deionized water three times, and thoroughly dried at 80°C . The dehydrated sample was mixed with KOH powder at a KOH/nanospheres mass ratio of 1:3. The mixture was then heat-treated at 700°C for 2 h in a tube furnace under flowing nitrogen for simultaneous carbonization and activation. The activated materials were repeatedly washed using 1 M HCl and deionized water until neutral, and then were dried at 80°C for 12 h (yield: 21%).

4.3 | Preparation of PC-NS

γ -CD (2.0 g) was dissolved in 120 ml deionized water and stirred at room temperature for 12 h. The subsequent HTC process, carbonization, and activation process were the same as those used for preparing the HPC-NS samples.

4.4 | Fabrication of working electrode and coin-type supercapacitors

The working electrode was prepared as follows: porous carbon nanospheres were mixed with acetylene black in an agate mortar. The homogeneous black powder was mixed with a PTFE suspension, together with a few drops of ethanol, and was then mounted on nickel foam (with a diameter of 1.4 cm). The mass ratio of the active material, acetylene black, and PTFE was 80:10:10. The carbon-loaded nickel foam was then pressed at 15 MPa. Finally, the molded electrodes were dried overnight in an oven at 80°C . Symmetric coin-type supercapacitors were constructed by assembling two pieces of the electrode with a cellulose film as a separator and 6 M KOH or 1 M Li_2SO_4 as the electrolyte. The volume of the electrolyte used in a single device was approximately 20 μl .

4.5 | Material characterization

The morphologies of the carbon nanospheres were examined using a JEOL 7500F SEM operating at 10 kV. To prepare samples for TEM inspection, the materials were embedded in epoxy resin and sliced using an ultramicrotome. TEM analysis was carried out using a JEOL JEM-2100F instrument. Nitrogen adsorption/desorption tests were performed by taking Brunauer-Emmett-Teller (BET) measurements using an ASAP-2010 surface area analyzer. The pore size distribution was estimated using the nonlocal density function theory (NLDFT) model. XRD patterns were obtained using a Bruker focus D8 diffractometer (40 kV, $\lambda = 0.15418 \text{ nm}$). Raman spectra were obtained using an HR800 spectrometer (HORIBA Jobin Yvon, wavelength: 633 nm). XPS analysis was performed on a Perkin-Elmer PHI 550 spectrometer with $\text{AlK}\alpha$ (1486.6 eV) as the x-ray source. Solid-state NMR analysis was performed using a Bruker Avance III HD 400 spectrometer equipped with 2.5 mm double-resonance magic-angle-spinning (MAS) probes, and the rotor was spun at 10 000 rpm. Specifically, to investigate the accessibility of the micropores of the obtained porous carbons using NMR spectroscopy, the carbon powder was degassed at 150°C for 3 h under vacuum, and 0.1 g of the degassed carbon was immersed in a 100 μl NaOH solution (6 M) for 12 h and then dried thoroughly prior to the measurements.

4.6 | Electrode density measurements

The packing density of the electrode material, ρ (g cm^{-3}), was measured by compressing a certain amount of the sample in a pressure mold (inner diameter of 10 mm),

without adding conductive carbon black and binder, under 10 MPa using a laboratory hydraulic machine. The density was calculated using the following equation: $\rho = 4m/(\pi d^2 h)$, where m is the mass of the sample (>0.5 g), d is the inner diameter of the pressure mold (10 mm), and h is the height of the sample after compression.

4.7 | Electrochemical characterization

EIS was performed in the frequency range of 100 kHz–0.01 Hz with an alternating current amplitude of 5 mV. CV and GCD tests were carried out using a CHI 760E instrument (Shanghai Chenhua Apparatus Co., Ltd.). Both three-electrode and two-electrode tests were performed. In the three-electrode test, porous carbon nanospheres were loaded on nickel foam and served as the working electrode; a Pt foil served as the counter electrode, and an Ag/AgCl electrode acted as the reference electrode. In the two-electrode test, coin-type symmetric supercapacitor devices were fabricated. The gravimetric capacitance of a single electrode tested using a three-electrode system, C_e ($F\ g^{-1}$), was calculated from the discharge curve according to the following equation:

$$C_e = \frac{I}{m \times (\Delta U / \Delta t)}, \quad (1)$$

where I is the constant charge/discharge current, Δt is the discharge time, ΔU is the potential window during the discharge process (excluding the voltage drop), and m is the mass of the active material on the working electrode. The volumetric capacitance of a single electrode was tested using a three-electrode system, C_V ($F\ cm^{-3}$) and was evaluated according to the following equation:

$$C_V = C_g \times \rho. \quad (2)$$

The gravimetric capacitance of a single electrode, C_g ($F\ g^{-1}$), was calculated from the discharge curve data using the two-electrode system according to the following equation:

$$C_g = 4 \times \frac{I}{2m \times (\Delta U / \Delta t)}. \quad (3)$$

The gravimetric energy density of the device, E_g ($Wh\ kg^{-1}$), was estimated using the following equation:

$$E_g = \frac{1}{28.8} C_g (\Delta U)^2. \quad (4)$$

The gravimetric power density of the device, P_g ($W\ kg^{-1}$), was calculated using the following equation:

$$P_g = \frac{3600 E_g}{\Delta t}. \quad (5)$$

ACKNOWLEDGMENTS

This work was supported by the Shenzhen Government's Plan of Science and Technology (JCYJ20190808121407676 and 20200813142301001), the Natural Science Foundation of Guangdong (2020A1515011127), the Natural Science Foundation of China (22178223), and the Shenzhen University Initiative Research Program (Grant No. 2019005).

CONFLICT OF INTEREST

The authors declare no conflict of interest.

ORCID

Lei Yao  <https://orcid.org/0000-0001-5289-7970>

Zijian Zheng  <https://orcid.org/0000-0002-6653-7594>

REFERENCES

- Shang J, Huang Q, Wang L, Yang Y, Li P, Zheng Z. Soft hybrid scaffold (SHS) strategy for realization of ultrahigh energy density of wearable aqueous supercapacitors. *Adv Mater.* 2019;30(4):1907088.
- Huang Q, Yang Y, Chen R, Wang X. High performance fully paper-based all-solid-state supercapacitor fabricated by a papermaking process with silver nanoparticles and reduced graphene oxide-modified pulp fibers. *EcoMat.* 2021;3:e12076.
- Liu L, Zhao H, Lei Y. Advances on three-dimensional electrodes for micro-supercapacitors: a mini-review. *InfoMat.* 2019;1(1):74-84.
- Wang R, Yao M, Niu Z. Smart supercapacitors from materials to devices. *InfoMat.* 2020;2:113-125.
- Simon P, Gogotsi Y, Dunn B. Where do batteries end and supercapacitors begin? *Science.* 2014;343:1210-1211.
- Borchardt L, Leistenschneider D, Haase J, Dvoyashkin M. Revisiting the concept of pore hierarchy for ionic transport in carbon materials for supercapacitors. *Adv Energy Mater.* 2018;8(24):1800892.
- Wang D, Li F, Liu M, Lu GQ, Cheng H-M. 3D aperiodic hierarchical porous graphitic carbon material for high-rate electrochemical capacitive energy storage. *Angew Chem Int Ed.* 2008;120:373-376.
- Kurosaki F, Koyanaka H, Tsujimoto M, Imamura Y. Shape-controlled multi-porous carbon with hierarchical micro-meso-macro pores synthesized by flash heating of wood biomass. *Carbon.* 2008;46(6):850-857.
- Hona RK, Karki SB, Ramezanipour F. Self-template synthesis of multiheteroatom codoped porous carbon with rational mesoporosity from traditional chinese medicine dregs for high-performance supercapacitors. *ACS Sustain Chem Eng.* 2020;8:11667-11681.
- Wang M, Zhou X, Wang S, Xie X, Wang Y, Su X. Fabrication of bioresource-derived porous carbon-supported iron as an efficient oxidase mimic for dual-channel biosensing. *Anal Chem.* 2021;93:3130-3137.

11. Zhang S, Xia W, Yang Q. Core-shell motif construction: Highly graphitic nitrogen-doped porous carbon electrocatalysts using MOF-derived carbon@COF heterostructures as sacrificial templates. *Chem Eng J*. 2020;396:125154.
12. Li J, Xia W, Tang J, et al. MOF nanoleaves as new sacrificial templates for the fabrication of nanoporous Co-N_x/C electrocatalysts for oxygen reduction. *Nanoscale Horiz*. 2019;4(4):1006-1013.
13. Hou J, Cao C, Idrees F, Ma X. Hierarchical porous nitrogen-doped carbon nanosheets derived from silk for ultrahigh-capacity battery anodes and supercapacitors. *ACS Nano*. 2013;9(3):2556-2564.
14. Bu Y, Sun T, Cai Y, et al. Compressing carbon nanocages by capillarity for optimizing porous structures toward ultrahigh-volumetric-performance supercapacitors. *Adv Mater*. 2017;29:1700470.
15. Yao L, Wu Q, Zhang P, et al. Scalable 2D hierarchical porous carbon nanosheets for flexible supercapacitors with ultrahigh energy density. *Adv Mater*. 2018;30:1706054.
16. Vasilyev OA, Kornyshev AA, Kondrat S. Connections matter: on the importance of pore percolation for nanoporous supercapacitors. *ACS Appl Energy Mater*. 2019;2(8):5386-5390.
17. Dutta S, Bhaumik A, Wu KC-W. Hierarchically porous carbon derived from polymers and biomass: effect of interconnected pores on energy applications. *Energy Environ Sci*. 2014;7(11):3574-3592.
18. Bai Q, Shen Y, Asoh T-A, Li C, Dan Y, Uyama H. Controlled preparation of interconnected 3D hierarchical porous carbons from bacterial cellulose-based composite monoliths for supercapacitors. *Nanoscale*. 2020;12:15261-15274.
19. Ban C-L, Xu Z, Wang D, Liu Z, Zhang H. Porous layered carbon with interconnected pore structure derived from reed membranes for supercapacitors. *ACS Sustain Chem Eng*. 2019;7(12):10742-10750.
20. An SY, Schon TB, McAllister BT, Seferos DS. Design strategies for organic carbonyl materials for energy storage: small molecules, oligomers, polymers and supramolecular structures. *EcoMat*. 2020;2:e12055.
21. Li Y, Du YF, Sun GH, et al. Self-standing hard carbon anode derived from hyper-linked nanocellulose with high cycling stability for lithium-ion batteries. *EcoMat*. 2021;3:e12091.
22. Min J, Wen X, Tang T, et al. A general approach towards carbonization of plastic waste into a well-designed 3D porous carbon framework for super lithium-ion batteries. *Chem Commun*. 2020;56:9142-9145.
23. Tan H, Tang J, Kim J, et al. Rational design and construction of nanoporous iron- and nitrogen-doped carbon electrocatalysts for oxygen reduction reaction. *J Mater Chem A*. 2019;7(4):1380-1393.
24. Wang J, Kaskel S. KOH activation of carbon-based materials for energy storage. *J Mater Chem*. 2012;22(45):23710-23725.
25. Mo Z, Yang W, Gao S, et al. Efficient oxygen reduction reaction by a highly porous, nitrogen-doped carbon sphere electrocatalyst through space confinement effect in nanopores. *J Adv Ceram*. 2021;10(4):714-728.
26. Ye X, Chen Z, Ai S, et al. Porous SiC/melamine-derived carbon foam frameworks with excellent electromagnetic wave absorbing capacity. *J Adv Ceram*. 2019;8(4):479-488.
27. Xie J, Li BQ, Peng HJ, et al. From supramolecular species to self-templated porous carbon and metal-doped carbon for oxygen reduction reaction catalysts. *Angew Chem Int Ed Engl*. 2019;58:4963-4967.
28. Tang J, Liu J, Li C, et al. Synthesis of nitrogen-doped mesoporous carbon spheres with extra-large pores through assembly of diblock copolymer micelles. *Angew Chem Int Ed*. 2015;54:588-593.
29. Fang Y, Gu D, Zou Y, et al. A low-concentration hydrothermal synthesis of biocompatible ordered mesoporous carbon nanospheres with tunable and uniform size. *Angew Chem Int Ed*. 2010;49:7987-7991.
30. Fei H-F, Li W, Bhardwaj A, Nuguri S, Ribbe A, Watkins JJ. Ordered nanoporous carbons with broadly tunable pore size using bottlebrush block copolymer templates. *J Am Chem Soc*. 2019;141:17006-17014.
31. Liu J, Yang T, Wang D-W, Lu GQ, Zhao D, Qiao SZ. A facile soft-template synthesis of mesoporous polymeric and carbonaceous nanospheres. *Nat Commun*. 2013;4:2798.
32. Liu T, Zhou Z, Guo Y, Guo D, Liu G. Block copolymer derived uniform mesopores enable ultrafast electron and ion transport at high mass loadings. *Nat Commun*. 2019;10:675.
33. Deng L, Young RJ, Kinloch IA, et al. Supercapacitance from cellulose and carbon nanotube nanocomposite fibers. *ACS Appl Mater Interfaces*. 2013;5:9983-9990.
34. Li J, Ni X, Leong K. Block-selected molecular recognition and formation of polypseudorotaxanes between poly(propylene oxide)-poly(ethylene oxide)-poly(propylene oxide) triblock copolymers and alpha-cyclodextrin. *Angew Chem Int Ed*. 2003;42:69-72.
35. Chen Y, Li X, Liao W, et al. High efficiency nitrogen doping and single atom cobalt anchoring via supermolecules for oxygen reduction electrocatalysis. *J Mater Chem A*. 2021;9(6):3398-3408.
36. Hulicova-Jurcakova D, Seredych M, Lu GQ, Bandosz TJ. Combined effect of nitrogen-and oxygen-containing functional groups of microporous activated carbon on its electrochemical performance in supercapacitors. *Adv Funct Mater*. 2009;19(3):438-447.
37. He Y, Zhang Y, Li X, et al. Capacitive mechanism of oxygen functional groups on carbon surface in supercapacitors. *Electrochim Acta*. 2018;282:618-625.
38. Chen C-M, Zhang Q, Zhao X-C, et al. Hierarchically aminated graphene honeycombs for electrochemical capacitive energy storage. *J Mater Chem*. 2012;22(28):14076-14084.
39. Lin X-Q, Yang N, Lü Q-F, Liu R. Self-nitrogen-doped porous biocarbon from watermelon rind: a high-performance supercapacitor electrode and its improved electrochemical performance using redox additive electrolyte. *Energy Technol*. 2019;7:1800628.
40. Deschamps M, Gilbert E, Azais P, et al. Exploring electrolyte organization in supercapacitor electrodes with solid-state NMR. *Nat Mater*. 2013;12:351-358.
41. Griffin JM, Forse AC, Tsai WY, Taberna PL, Simon P, Grey CP. In situ NMR and electrochemical quartz crystal microbalance techniques reveal the structure of the electrical double layer in supercapacitors. *Nat Mater*. 2015;14:812-819.

42. Forse AC, Griffin JM, Merlet C, et al. NMR study of ion dynamics and charge storage in ionic liquid supercapacitors. *J Am Chem Soc.* 2015;137:7231-7242.
43. Chen C, Yu D, Zhao G, et al. Three-dimensional scaffolding framework of porous carbon nanosheets derived from plant wastes for high-performance supercapacitors. *Nano Energy.* 2016;27:377-389.
44. Zhu J, Xu D, Qian W, Zhang J, Yan F. Heteroatom-containing porous carbons derived from ionic liquid-doped alkali organic salts for supercapacitors. *Small.* 2016;12:1935-1944.
45. Wang X, Li HD, Liu P. Well-defined aniline-triphenylamine copolymer nanotubes: preparation, photoluminescent, and electrochemical properties. *Electrochim Acta.* 2014;125:630-636.
46. Lin T, Chen W, Liu F, et al. Nitrogen-doped mesoporous carbon of extraordinary capacitance for electrochemical energy storage. *Science.* 2015;350:1508-1513.
47. Ogino S, Itoh T, Mabuchi D, et al. In situ electrochemical Raman spectroscopy of air-oxidized semiconducting single-walled carbon nanotube bundles in aqueous sulfuric acid solution. *J Phys Chem C.* 2016;120(13):7133-7143.
48. Yan J, Wang Q, Lin CP, Wei T, Fan ZJ. Interconnected frameworks with a sandwiched porous carbon layer/graphene hybrids for supercapacitors with high gravimetric and volumetric performances. *Adv Energy Mater.* 2014;4(13):1400500.
49. Jiang LL, Sheng LZ, Long CL, Fan ZJ. Densely packed graphene nanomesh-carbon nanotube hybrid film for ultrahigh volumetric performance supercapacitors. *Nano Energy.* 2015;11:471-480.
50. Lu XJ, Dou H, Yang SD, et al. Fabrication and electrochemical capacitance of hierarchical graphene/polyaniline/carbon nanotube ternary composite film. *Electrochim Acta.* 2011;56(25):9224-9232.
51. Yuan DS, Chen JX, Zeng JH, Tan SX. Preparation of monodisperse carbon nanospheres for electrochemical capacitors. *Electrochem Commun.* 2008;10(7):1067-1070.
52. Wang Q, Yan J, Fan Z. Nitrogen-doped sandwich-like porous carbon nanosheets for high volumetric performance supercapacitors. *Electrochim Acta.* 2014;146:548-555.
53. Yu M, Wang Z, Zhang H, et al. Amino functionalization optimizes potential distribution: a facile pathway towards high-energy carbon-based aqueous supercapacitors. *Nano Energy.* 2019;65:103987.
54. Yu M, Lin D, Feng H, Zeng Y, Tong Y, Lu X. Boosting the energy density of carbon-based aqueous supercapacitors by optimizing the surface charge. *Angew Chem Int Ed.* 2017;56:1-6.
55. Xu Y, Lin Z, Zhong X, et al. Holey graphene frameworks for highly efficient capacitive energy storage. *Nat Commun.* 2014;5:4554.
56. Fan XM, Yu C, Yang J, et al. A layered-nanospace-confinement strategy for the synthesis of two-dimensional porous carbon nanosheets for high-rate performance supercapacitors. *Adv Energy Mater.* 2014;5(7):1401761.
57. Bichat MP, Raymundo-Pinero E, Beguin F. High voltage supercapacitor built with seaweed carbons in neutral aqueous electrolyte. *Carbon.* 2010;48(15):4351-4361.
58. Fic K, Lota G, Meller M, Frackowiak E. Novel insight into neutral medium as electrolyte for high-voltage supercapacitors. *Energ Environ Sci.* 2012;5(2):5842-5850.
59. He M, Fic K, Frackowiak E, Novak P, Berg EJ. Ageing phenomena in high-voltage aqueous supercapacitors investigated by in situ gas analysis. *Energ Environ Sci.* 2016;9(2):623-633.
60. Zhao J, Jiang Y, Fan H, et al. Porous 3D few-layer graphene-like carbon for ultrahigh-power supercapacitors with well-defined structure-performance relationship. *Adv Mater.* 2017;29:1604569.
61. Tiwari VK, Chen Z, Gao F, Gu Z, Sun X, Ye Z. Synthesis of ultra-small carbon nanospheres (<50 nm) with uniform tunable sizes by a convenient catalytic emulsion polymerization strategy: superior supercapacitive and sorption performance. *J Mater Chem A.* 2017;5(24):12131-12143.
62. Zhang N, Liu F, Xu S-D, Wang F-Y, Yu Q, Liu L. Nitrogen-phosphorus Co-doped hollow carbon microspheres with hierarchical micro-meso-macroporous shells as efficient electrodes for supercapacitors. *J Mater Chem A.* 2017;5(43):22631-22640.

SUPPORTING INFORMATION

Additional supporting information may be found in the online version of the article at the publisher's website.

How to cite this article: Yao L, Lin J, Chen Y, et al. Supramolecular-mediated ball-in-ball porous carbon nanospheres for ultrafast energy storage. *InfoMat.* 2022;4(4):e12278. doi:10.1002/inf2.12278